Ceramics-Silikáty 67 (4), 543-550 (2023)
www.ceramics-silikaty.cz doi: 10.13168/cs.2023.0053

THE VARIATION IN MICROSTRUCTURE OF LITHIUM DISILICATE GLASS AND GLASS-CERAMICS

#HUYNH NGOC MINH*, **, NGUYEN VU UYEN NHI*, **, KIEU DO TRUNG KIEN*, **, #DO QUANG MINH*, **

*Department of Silicate Materials, Faculty of Materials Technology, Ho Chi Minh City University of Technology (HCMUT), 268 Ly Thuong Kiet Street, District 10, Ho Chi Minh City, Vietnam
**Vietnam National University Ho Chi Minh City, Linh Trung Ward, Thu Duc City, Ho Chi Minh City, Vietnam

#E-mail: hnminh@hcmut.edu.vn, mnh_doquang@hcmut.edu.vn

Submitted October 15, 2023; accepted November 14, 2023

Keywords: Lithium disilicate, Glass-ceramic, Dental material, X-ray photoelectron spectroscopy

The microstructural transformation from lithium disilicate glass with the chemical composition (mol. %) SiO_2 (65.35), Li_2O (30.23), K_2O (1.76), Al_2O_3 (1.77), and P_2O_5 (0.89) to a glass-ceramic (GC) was detailed in this study. The X-ray diffraction and Fourier Transform Infrared Spectroscopic analysis detected the crystalline phases in the GC sample, including lithium disilicate, lithium metasilicate, and traces of other crystals. The scanning electron microscopic images illustrated the characteristic interlocking microstructure of the lithium disilicate GC. The $[SiO_4]^{4-}$ tetrahedra arranged and linked together through n shared O^{2-} vertices to create a characteristic structural framework of each silicate phase (symbolised as Q^n species). The examination of the Si 2p and O 1s high-resolution XPS spectra revealed that the structure of the GC sample possessed a broader distribution of Q^n species and an increase in the proportion of low n-index Q^n species compared to the glass sample. The Si $2p_{3/2}$ peak position of the glass sample shifted to a 0.26 eV lower binding energy level than that of the GC sample. This change demonstrates that lithium silicate glass readily crystallises into GC, the more stable state. The results are the arguments to determine the crystallisation mechanism and structural variation of the studied lithium disilicate system.

INTRODUCTION

Glass-ceramics (GCs) are ceramic materials made by the controlled crystallisation of glass. GCs consist of fine, uniform, dispersed crystals in the remaining glass matrix with almost no pores. These materials possess high strength and tailored unique properties. In the field of dental materials, GCs that have the main crystalline phase of lithium disilicate ($Li_2O{\cdot}2SiO_2$ – LS_2) can match natural tooth performance and meet modern porcelain prosthetic technologies, such as powder sintering, hot-press casting, Computer-aided design/Computer-aided manufacturing (CAD-CAM) processing, etc. [1–4]. LS_2 GC, in particular, has a much higher flexural strength than the parent glass due to the presence of LS_2 microcrystals, which is an orthorhombic phyllosilicate with a layered structure [5, 6].

LS_2 GC has a prosperous chemical composition that includes various components apart from the primary SiO_2 and Li_2O components, which are used to design its microstructure and properties for different dental applications. Moreover, the fabrication process for making GC dental restoration parts from LS_2 glass is complex and involves several stages. Based on the chemical composition and controlled crystallisation process, the phase composition of LS_2 GC usually comprises the main crystal phase LS_2, lithium metasilicate ($Li_2O{\cdot}SiO_2$ - LS), Li_3PO_4, cristobalite (SiO_2), etc., and the remaining glass phase.

The basic structural unit of silicate compounds in the crystalline or glassy state is the $[SiO_4]^{4-}$ tetrahedron. These tetrahedra can exist independently or link together through shared oxygen vertices known as non-bridging oxygens (NBOs). The symbol for the silicon types of the different bonded $[SiO_4]^{4-}$ tetrahedra is Q^n, where n ($0 \leq n \leq 4$) represents the number of bridging oxygens surrounding the silicon atom at the tetrahedral vertices connecting the adjacent tetrahedra. In LS_2 GCs, LS is a metastable phase that forms at low temperatures before the crystallisation of LS_2 [1, 7, 8]. The LS crystal (SiO_2/Li_2O = 1) possesses a Q^2 chain structure (chain silicate structure). On the other hand, the LS_2 crystal

(SiO_2/Li_2O = 2) possesses a Q^3 layer structure (layer silicate structure/phyllosilicate) [7]. The microstructural changes during the fabrication process determine the properties of the resulting materials. In recent years, extensive research in glass-ceramic science and engineering has focused on comprehending the crystallisation process from the glass phase [9–11]. Spectroscopic methods have been beneficial in this regard. The X-ray diffraction (XRD) method is used to determine the phase composition, lattice parameters, crystallinity ratio, and crystal size of the materials. The Fourier transform infrared (FTIR) spectroscopy analyses the material's infrared (IR) absorption peaks, revealing the bond of the functional groups to explain the structural transformations of GC materials during the heat treatment stages [12–14]. X-ray photoelectron spectroscopy (XPS) is an effective analytical technique for studying the elemental surface composition (determining binding energies of atomic orbitals), bond nature, and oxidation state of the cations in the material [14–16]. Many previous studies have used XPS to show the binding energy differences of elements in glasses and GC.

In this study, the crystalline phases in the material were determined using an XRD analysis. The FTIR analysis identified the bonds or functional groups representing the Q^n species. Most importantly, the binding energy of the atomic orbitals in Q^n was quantified by XPS. The combination of spectroscopic analyses and Scanning Electron Microscopy (SEM) results helped to discover the crystallisation mechanism and the microstructural variation of the lithium disilicate glass and GC.

EXPERIMENTAL

Materials

The glass batch was prepared by mixing amounts of raw materials, including precipitated amorphous silica (Rhodia Silica Korea Co., Ltd-Korea); Li_2CO_3, $Al(OH)_3$, KH_2PO_4, K_2CO_3 (Analytical Reagent grade, Xilong Scientific Co., Ltd, China). The ratio of the mixture was carefully calculated to ensure that the glass sample had a specific chemical composition with a ratio of oxides in mol. %: SiO_2 (65.35), Li_2O (30.23), K_2O (1.76), Al_2O_3 (1.77) and P_2O_5 (0.89). SiO_2 and Li_2O are the two primary components; K_2O and Al_2O_3 improve the chemical stability; and P_2O_5 acts as a heterogeneous nucleation agent for the volumetric crystallisation process. The ingredients were thoroughly mixed and melted in a platinum crucible at 1450 °C for 1.5 hours before being poured into a preheated steel mould to form a cylinder (H = 20mm, Φ = 12mm). The glass blocks were then annealed in the kiln at 450 °C for 1 hour before cooling naturally to reduce the stress inside the glass. The glass sample was denoted M-Glass.

The heating regime for the M-Glass crystallisation and formed dental GC pieces was determined based on a differential thermal analysis (DTA) [17]. Firstly, The M-Glass blocks were two-stage heat treated at 600 °C for 90 minutes and 720 °C for 30 minutes in an electric furnace (Magma – Renfert – Germany) to create GC ingots. Secondly, these ingots were hot-pressed at 965 °C in an EP3000 furnace using the lost-wax casting process to create the dental GC products denoted M-GC.

Structural analysis methods

The M-Glass and M-GC samples for the XRD, FTIR, and XPS analyses were ground using an alumina ceramic mortar until the fine-grained powder could pass through a 63 μm sieve. The resulting powders were then dried at 110 °C until their weight remained consistent and cooled in a desiccator. The XRD analysis was performed on a D8 Bruker instrument with the following measurement conditions: KαCu = 1.5406 Å, 2θ = 10 –70°, step and scan rate 0.01°/16.38 s.

The FTIR spectra were recorded using a NICOLET 6700 device (Thermo Scientific). The samples for the FTIR analysis were compressed into pellets with KBr (the powder was mixed with KBr in a ratio of 1 mg of the sample to 100 mg of KBr and pressed with a high pressure of 1.5 tonnes to create a transparent sample pellet) with the number of scans: 32 times, the speed: 0.6329 $m \cdot s^{-1}$ at room temperature in the infrared range from 400 - 4000 cm^{-1}.

The XPS was analysed on an AXIS Nova (XPS) surface analysis spectrometer (Shimadzu-Kratos) using Al Kα radiation with hν = 1486.6 eV, the base pressure of the chamber was lower than 10^{-8} Pa, and the swell time was 0.1 s for the wide-scan and 0.1 - 0.6 s for the high-resolution scan. High-resolution Si 2p and O 1s XPS spectra were studied in this paper.

The microstructure characterisations of the fracture surface of the samples before (M-Glass) and after the (M-GC) crystallisation process were performed using a Philips XL30 scanning electron microscope. The fracture samples were cleaned in an ultrasonic bath with deionised water for 5 minutes, dried, and then sputtered with Au before being examined by SEM.

RESULTS AND DISCUSSION

Result of the XRD analysis

In Figure 1, the X-ray diffraction patterns of the M-Glass and M-GC samples, and the Joint Committee on Powder Diffraction Standards (JCPDS) pattern of the crystalline phases present in the M-GC are displayed. The XRD pattern of the M-Glass shows the characteristic form of an amorphous phase without any peak for the presence of the crystalline phase. It means that the M-Glass was completely vitrified by melting its

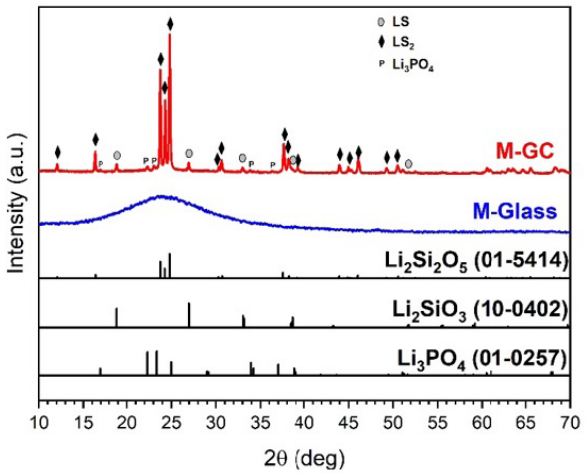

Figure 1. Results of the XRD analysis of the M-Glass and M-GC.

raw material mixture. The pattern of the M-GC exhibits distinctive peaks for the crystalline phases, with LS_2 constituting the principal component alongside LS and a small proportion of Li_3PO_4. The presence of minute traces of Li_3PO_4 points towards the usage of P_2O_5, acting as a heterogeneous nucleating agent, which has been previously discussed [17, 18], as well as in the works of other authors [5, 19–21]. These results confirm that the M-Glass has been transformed into the glass-ceramic material (M-GC) after the heat treatment and hot-press processing.

SEM images

The SEM images of the fractured surfaces of the M-Glass and M-GC samples are presented in Figure 2. The SEM image of the M-Glass sample displays a flat surface without scattered phases, which is typical of a glass material's fractured surface. Meanwhile, the SEM image of the M-GC fractured surface shows a terraced topography with interlocking sheets and rod crystals. This glass-to-GC microstructural transformation predicts potential improvements in the strength and other properties of the material. Indeed, it was demonstrated in our previous publication's results when measuring the physicochemical properties of the M-GC [17].

FTIR spectra

The absorption peaks of the FTIR spectra provide insight into the material's characteristic bonds. Figure 3 presents the FTIR spectra of the M-Glass pre-

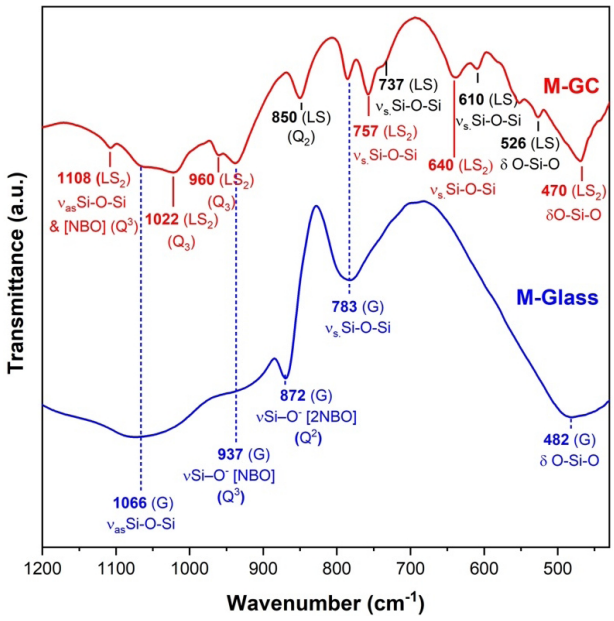

Figure 3. FTIR spectra of the M-Glass and M-GC.
Notation: *v*: Stretching vibration, *δ*: deformations/ Bending vibrations, *s*.: symmetric, *as*.: asymmetric.

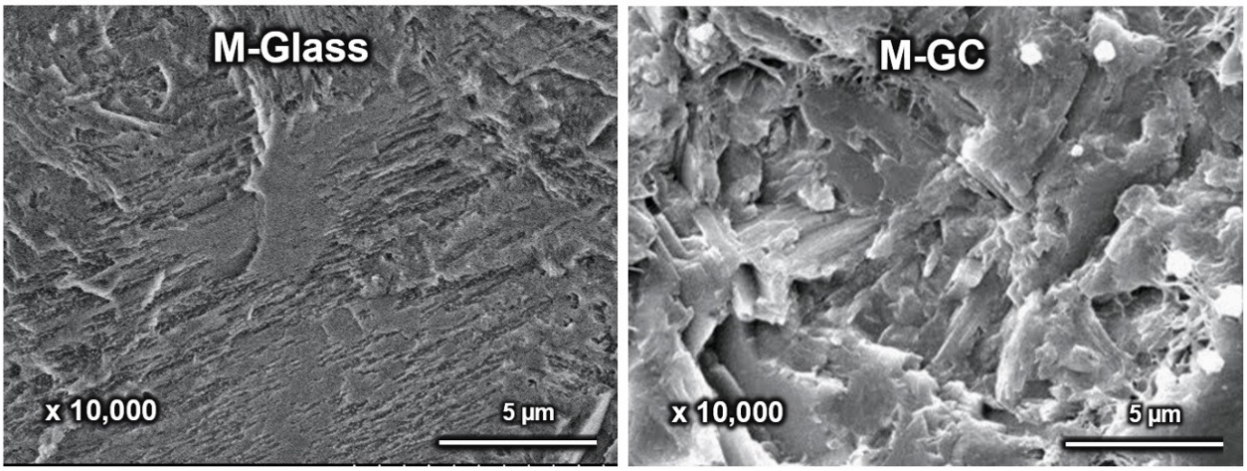

Figure 2. SEM images of the M-Glass and M-GC.

crystallisation and M-GC post-crystallisation samples. The M-Glass spectrum displayed broad absorption bands and obtuse peaks, whereas many sharp peaks were visible in the M-GC spectrum. The results indicated significant alteration in the phase composition and structure of the material.

The FTIR spectrum of M-Glass exhibits discernible absorption bands that correspond to the vibrational modes of the 4-corner shared $[SiO_4]^{4-}$ tetrahedra (Q^4 species) in a silicate glass structure: the band at 482 cm^{-1} presents the bending vibration δ O-Si-O [22] corresponding the bonding of central Silicon atom with oxygen atoms at four corners of $[SiO_4]^{4-}$; asymmetric stretching ν_{as} as Si-O-Si at 1066 cm^{-1} and symmetric stretching ν_s Si-O-Si at 783 cm^{-1} [14, 22, 23] correspond the bridging oxygens (BOs) linking the $[SiO_4]^{4-}$ tetrahedra together. In addition, the band at 937 cm^{-1} is characteristic of ν Si-O-[NBO] [14, 22] showing that there are $[SiO_4]^{4-}$ tetrahedra with one non-bridging oxygen (NBO) corner (Q^3 species); the peak at 872 cm^{-1} is typical for ν Si-O-[2NBO] [14] belonging to $[SiO_4]^{4-}$ tetrahedra with a two NBO corner (Q^2 species) in the glass network. The absorption bands on the spectrum of M-Glass clearly showed the characteristic structure of silicate glass with modified ions (Li^+, K^+) along with an intermediate ion (Al^{3+}) in the composition. These ions interrupted the continuum of the glass network by breaking some linking between $[SiO_4]^{4-}$ tetrahedra, resulting in the attendance of NBOs (Q^3 and Q^2 species).

The FTIR spectrum of M-GC, as depicted in Figure 2, features a distinct cluster of absorption peaks that are characteristic of LS_2 crystalline bonds [22, 23]: the peak at 470 cm^{-1} corresponds to bending vibration ν O-Si-O (belonging to the bonding of Si atom with oxygen vertices); the peaks at 640, 757, and 1108 cm^{-1} correspond to the stretching vibration ν Si-O-Si (belonging to the link of the BO located tetrahedral corner); the peaks at 1108, 1022, and 960 cm^{-1} correspond to the stretching vibration ν Si-O-[NBO] in the layer structure (Q^3 species). In addition, a group of absorption peaks characteristic of the bonding of LS crystals is also present [23]: the peaks at 526 and 552 cm^{-1} correspond to ν O-Si-O; at 610 and 737 cm^{-1} corresponds to ν Si-O-Si; the peak at 850 cm^{-1} corresponds to ν Si-O- [2NBO] in the chain structure (Q^2 species). Whereas the absorption peaks at 1066, 937, and 783 cm^{-1} that characterise the bonds in the glass phase (residual after crystallisation) also exist in the M-GC spectrum.

LS_2, LS crystal, and residue glass phases were detected on the glass-ceramic FTIR spectrum, clearly showing types of Q^n species. Nevertheless, the mechanism of network structure transformation to form these crystalline phases during crystallisation still needs to be clarified.

XPS analysis

Figure 4 illustrates the XPS broad spectra of the M-Glass and M-GC samples. The sharp peaks at the different binding energies correspond to the O Auger, O 1s, C 1s, Si 2s, and Si 2p. A C 1s peak is visible in all the XPS wide-scan spectra, even if the sample does not contain carbon. The peak arises due to the absorption of dusty hydrocarbon impurities, ethanol, organic matter, and the low environmental vacuum, resulting in unexpected carbon. However, this peak does not impact the analysis of the findings. In many XPS studies [14–16, 24–26], including this study, the C 1s was set at 284.6 eV. This value was used as the reference for calibrating the binding energy values on the XPS spectra.

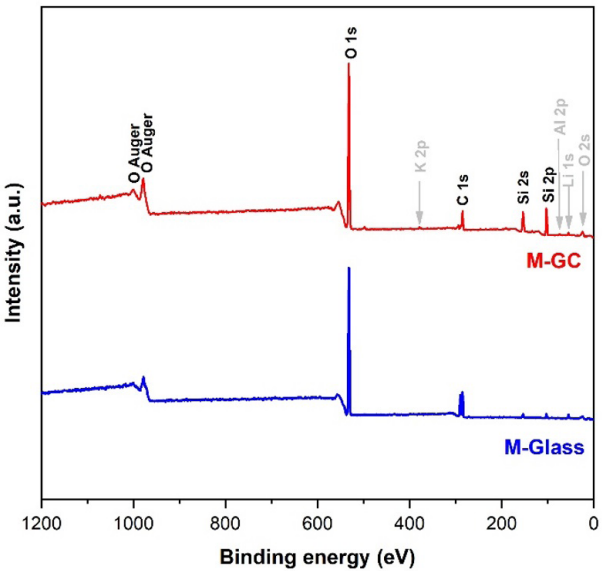

Figure 4. XPS broad spectra of the M-Glass and M-GC.

The results of the broad spectrum XPS analysis of the M-Glass and M-GC after calibration are shown in Figure 4. The peaks of K 2p (located in the range of binding energies 302 - 287 eV), Al 2p (78 - 68 eV), and Li 1s (56 - 54 eV) exhibit very low intensity. According to Buchner [27], although Li in the LS_2 GC systems has a high content (33.33 mol. %), the detection of Li 1s (48 - 62 eV) by XPS analysis in these materials processed at high temperatures gives a fragile signal. Hence, there is almost no characteristic peak appearance of Li 1s on the obtained XPS spectra. Similarly, Al_2O_3 (1.77 mol. %), K_2O (1.76 mol. %), and P_2O_5 (0.89 mol. %) are components with a relatively small content and are usually soluble in the glass phase. Hence, the peaks of K 2p, Al 2p, P 2p have very low intensity, which is consistent with the results of the broad spectrum XPS analysis of four commercial LS_2 GC products in the study conducted by França et al. [28]. For the analysis

of silicate material structure changes, high-resolution XPS spectroscopy was performed in the binding energy regions corresponding to Si 2p and O 1s (presented in Figure 5).

The high-resolution photoelectron peaks exhibit distinct differences that indicate a significant change in the structural configuration from the glass state to the GC state. When the peaks are asymmetrical, with inflection points or shoulder regions, it suggests the superposition of multiple peaks. The Si 2p spectrum comprises the contributions of Si $2p_{1/2}$ and Si $2p_{3/2}$, while the O 1s spectrum includes contributions from all the BOs and NBO in the glass and crystalline phases. Therefore, Si 2p and O 1s spectra were deconvoluted into Gaussian peaks using Origin software.

High resolution Si 2p XPS spectra

The Si 2p spectrum comprises one or more pairs of peaks related to pairs of Si $2p_{1/2}$ and Si $2p_{3/2}$ rotating atomic orbitals. The peak of Si $2p_{1/2}$ appears at a higher binding energy than that of Si $2p_{3/2}$. In the Si 2p XPS spectra of silicate minerals and glasses, the intensity of the Si $2p_{1/2}$ peak is half that of the Si $2p_{3/2}$ peak (measured by peak area) [16, 24, 27]. The distance between the two peaks ranges from approximately 0.617 eV [24] to 0.63 eV [28]. Therefore, the Si 2p high-resolution spectral peaks of M-Glass and M-GC were deconvoluted following the peak fit parameters: Baseline mode: constant, Auto parameter initialisation, max. Number of Iterations: 200, tolerance: $1E^{-6}$; with constraints:

1. The peak positions of Si $2p_{1/2}$ are observed to be at higher binding energy levels compared to those of Si $2p_{3/2}$. The distance between the two peak maxima is approximately 0.63 eV.
2. Si $2p_{1/2}$ peak area is half of Si $2p_{3/2}$ peak area.
3. The Full Width Half Maximum (FWHM) values of Si $2p_{1/2}$ and Si $2p_{3/2}$ peak are equal.

The Si 2p peak deconvolution results for M-Glass and M-GC are presented in Figure 6 and Table 1.

The fitting results exhibit the changes in the position and the FWHM of the Si $2p_{3/2}$ XPS peaks. Both glass and

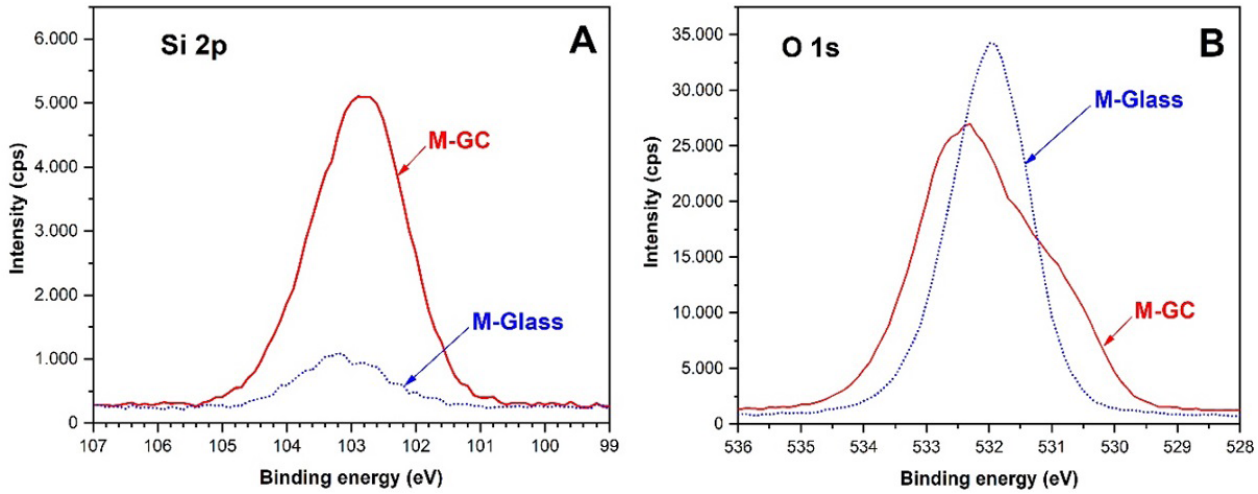

Figure 5. High resolution (A) Si 2p and (B) O 1s XPS spectra of the M-Glass and M-GC.

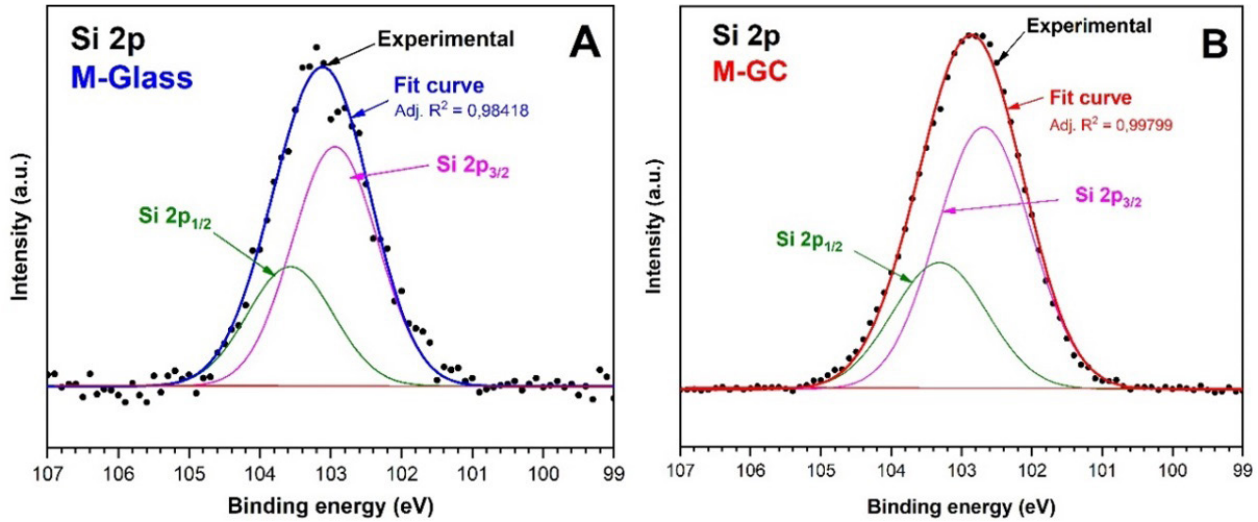

Figure 6. The deconvolution of the Si 2p high-resolution XPS spectra of the (A) M-Glass and (B) M-GC.

Table 1. Peak parameters obtained from deconvoluting the Si 2p XPS spectra.

Sample	Peak deconvolution	Peak position (eV)	FWHM (eV)
M-Glass	Si $2p_{1/2}$	103.57	1.42
	Si $2p_{3/2}$	102.94	1.42
M-GC	Si $2p_{1/2}$	103.31	1.58
	Si $2p_{3/2}$	102.68	1.58

GC states contain a variety of ratios of linked $[SiO_4]^{4-}$ tetrahedron (Q^n species) in the structure, as illustrated in Figure 6. Each Q^n species has a distinct peak position in the binding energy range of the Si 2p spectrum. The electron density of the Si atom depends on the number of BOs and NBOs bound to this Si atom. An increase in the NBO vertices increases the valence electron density of the Si atom at the tetrahedron centre, causing a shift in the Si 2p peak position to a lower binding energy level [16, 24].

After analysing the peak parameters obtained from the deconvoluted Si 2p XPS spectra of two samples, it was observed that M-GC had a broader Si $2p_{3/2}$ peak FWHM than the M-Glass. Additionally, the Si $2p_{3/2}$ peak position of M-GC shifted towards 102.68 eV, which is 0.26 eV lower than that of M-Glass. These findings indicate that the binding energy of the Si^{4+} ions decreased during the crystallization process, suggesting the favourable crystallisation ability of the lithium disilicate glass-ceramic system. Furthermore, the results suggest that the M-GC structure, after crystallisation, exhibits a broader distribution of Q^n species and an increased proportion of low n-valued Q^n species (Q^3 and Q^2 belong to the structure of LS_2 and LS crystals, respectively).

High resolution O 1s XPS spectra

The O 1s spectrum displays overlapping peaks comprising BOs and NBOs. The photoelectron peaks of the BOs in the Si-O-Si bond are located at a binding energy range of 532.7 – 531.8 eV. Meanwhile, the photoelectron peak of NBOs in the Si-O- bond was discovered at a lower binding energy range of 530.8 – 530.7 eV, with a difference of 1.5 – 2.0 eV from BO peaks due to the higher electron density on the NBOs [14], which is a consequence of the NBOs bonding to Li^+ ions (or other modifying ions) and the almost complete transfer of electrons of Li 1s to the unoccupied molecular orbitals of the NBO. The peak area ratio is used to measure the proportions of each type of BO and NBO in the material. Figure 7 and Table 2 display the O 1s peak deconvolution results for the M-Glass and M-GC.

Table 2. Peak parameter obtained from deconvoluting O 1s XPS spectra

Sample	Peak deconvolution	Peak position (eV)	FWHM (eV)	% of BO	% of O 1s
M-Glass	BO-1	532.22	1.95	43.0	43.0
	BO-2	531.91	1.27	57.0	57.0
M-GC	BO-1	532.63	1.05	9.2	8.0
	BO-2	532.26	2.10	90.8	79.0
	NBO	530.72	1.19	-	13.0

The O 1s spectrum of the M-Glass showed two peaks in the binding energy region of the BO. The BO-1 peak was found at a high binding energy of 532.22 eV (BO in Q^4 or Q^3), while the BO-2 peak was found at a lower binding energy level of 531.91 eV (BO in Q^3 or Q^2), with proportions of 43 % and 57 %, respectively. However, the O 1s spectrum of the M-GC displayed three peaks, which were more complex than that of the M-Glass. The BO-1 peak position (BO in Q^4 or Q^3)

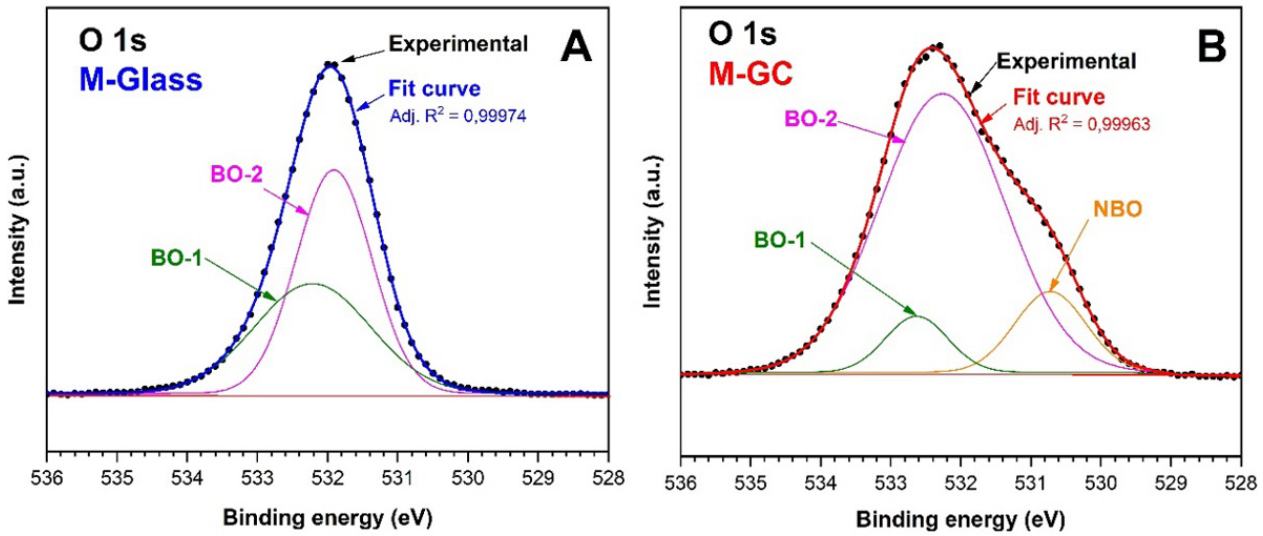

Figure 7. Results of the deconvolution of the Si 2p high-resolution XPS spectra of the (A) M-Glass and (B) M-GC.

shifted to a higher binding energy, and its proportion decreased to 8 %. The BO-2 peak position (BO in Q^3 or Q^2) also changed to a higher binding energy, but its proportion increased to 79 %. Notably, an NBO peak was observed at a low binding energy position of 530.72 eV, accounting for 13 % of the O 1s spectrum.

It has been observed that the crystallisation process of the LS_2 primary crystals (layer structure-Q^3) and LS crystals (chain structure-Q^2) from the glass phase (Q^4, Q^3, and Q^2) resulted in a significant increase in the amount of Q^3 species, Q^2 species, and NBOs, while decreasing the amount of Q^4 in the network structure of the material. Consequently, the mechanism of crystallisation and the microstructural changes in the lithium disilicate material can be effectively illustrated using the summary graphic provided below, based on the model of the structural units that exist in the two states of this material:

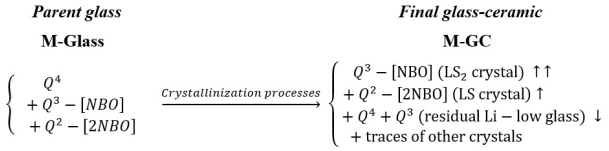

CONCLUSIONS

The crystallisation from the studied glass into glass-ceramic led to a significant change in the phase composition and microstructure. The XRD and SEM results showed that the phase composition of the M-GC consisted of LS_2, LS, and a trace of Li_3PO_4 crystal phases interlocking and dispersing in the residual glass matrix. The FTIR spectrum displayed the absorption peaks that characterise the vibrations of O-Si-O, Si-O-Si (involving bridging oxygens), and Si-O- (involving non-bridging oxygens) bonds in these silicate phases. The interpretation of Si 2p and O 1s high-resolution XPS spectra indicated that the GC structure had a broader distribution of Q^n species and an increased proportion of low n-valued Q^n species. The Si $2p_{3/2}$ peak position of M-GC shifted to a lower 0.26 eV than that of M-Glass. The reduction in the binding energy of the Si^{4+} ions during the crystallisation process implied the favourable crystallisation ability of the lithium disilicate glass-ceramic system. By examining spectral analysis results, the crystallisation mechanism and microstructural change of the studied lithium disilicate material can be clearly visualised.

Acknowledgements

We acknowledge Ho Chi Minh City University of Technology (HCMUT), VNU-HCM for supporting this study.

REFERENCES

1. Minh H. N., Vuong B. X., and Minh D. Q. (2018): Study of the Non-Isothermal Crystallization Kinetics of Lithium Disilicate Glass Ceramic. *Glass Physics and Chemistry, 44*(6), 524–530. doi:10.1134/S108765961901005X
2. Minh H. N., Minh D. Q. (2018): Ảnh hưởng của oxyt nguyên tố hiếm CeO_2, Nd_2O_3 đến sự phát huỳnh quang và màu sắc của gốm thủy tinh lithium disilicate dùng trong nha khoa (Effect of CeO_2, Nd_2O_3 on fluorescence and color of lithium disilicate dental glass-ceramic). Tạp Chí Hóa Học-Viện Hàn Lâm Khoa Học Công Nghệ Việt Nam, 56(3E12), 72–76.
3. Fu L., Engqvist H., Xia W. (2020): Glass–Ceramics in Dentistry: A Review. *Materials, 13*(5), 1049. doi:10.3390/ma13051049
4. Li R. W. K., Chow T. W., Matinlinna J. P. (2014): Ceramic dental biomaterials and CAD/CAM technology: State of the art. *Journal of Prosthodontic Research, 58*(4), 208-216. doi:10.1016/j.jpor.2014.07.003
5. Zheng X., Wen G., Song L., Huang X. X. (2008): Effects of P_2O_5 and heat treatment on crystallization and microstructure in lithium disilicate glass ceramics. *Acta Materialia, 56*(3), 549–558. doi:10.1016/j.actamat.2007.10.024
6. Von Clausbruch S. C., Schweiger M., Höland W., Rheinberger V. (2000): The effect of P_2O_5 on the crystallization and microstructure of glass-ceramics in the SiO_2–Li_2O–K_2O–ZnO–P_2O_5 system. *Journal of Non-Crystalline Solids, 263–264*, 388–394. doi:10.1016/S0022-3093(99)00647-X
7. Holand W., Beall G. H. (2012). *Glass Ceramic Technology.* John Wiley & Sons.
8. El-Meliegy E., van Noort R. (2011). *Glasses and Glass Ceramics for Medical Applications.* Springer Science & Business Media.
9. Zhang P., Li X., Yang J., Xu S. (2014): Effect of heat treatment on the microstructure and properties of lithium disilicate glass-ceramics. *Journal of Non-Crystalline Solids, 402*, 101–105. doi:10.1016/j.jnoncrysol.2014.05.023
10. Lien W., Roberts H. W., Platt J. A., Vandewalle K. S., Hill T. J., Chu T. M. G. (2015): Microstructural evolution and physical behavior of a lithium disilicate glass–ceramic. *Dental Materials, 31*(8), 928–940. doi:10.1016/j.dental.2015.05.003
11. Yan J., Liu X., Wu X., Wu X., Zhang Y., Li B. (2023): Microstructure and Mechanical Properties of $Li_2Si_2O_5$ Whisker-Reinforced Glass-Ceramics. *Frontiers in Materials, 9*, 849601.doi:10.3389/fmats.2022.849601
12. Mirhadi B., Mehdikhani B. (2011): Investigation of optical absorbance and crystallization of vanadium oxide in glasses. *Journal of Optoelectronics and Advanced Materials, 13*(5), 679-683.
13. El-Damrawi G., Hassan A. M., Ramadan R., El-Jadal S. (2016): Nuclear Magnetic Resonance and FTIR Structural Studies on Borosilicate Glasses Containing Iron Oxide. *Scientific Research, 06*(04), 47-56. doi:10.4236/njgc.2016.64006
14. Serra J. et al. (2003): FTIR and XPS studies of bioactive silica based glasses. *Journal of Non-Crystalline Solids, 332*(1–3), 20-27. doi:10.1016/j.jnoncrysol.2003.09.013
15. Mekki A. (2005): X-ray photoelectron spectroscopy of CeO_2–Na_2O–SiO_2 glasses. *Journal of Electron Spectroscopy and Related Phenomena, 142*(1), 75-81. doi:10.1016/j.

elspec.2004.09.001

16. Sawyer R., Nesbitt H. W., Secco R. A. (2012): High resolution X-ray Photoelectron Spectroscopy (XPS) study of K_2O–SiO_2 glasses: Evidence for three types of O and at least two types of Si. *Journal of Non-Crystalline Solids, 358*(2), 290-302. doi:10.1016/j.jnoncrysol.2011.09.027
17. Minh H. N., Minh D. Q., Hung D. H. T., Khoi N. T. (2017): Effects of Nd_2O_3 on the crystallization and properties of glass ceramic in Li_2O–K_2O–Al_2O_3–SiO_2–P_2O_5 system. Vietnam Journal of Science and Technology, 55(1B), 238-238.
18. Minh H. N., Hanh N. X., Van V. N. H., Minh D. Q. (2015): Ảnh hưởng của chế độ nhiệt đến sự kết tinh và cơ tính của gốm thủy tinh nha khoa lithium disilicate tạo hình bằng phương pháp ép nóng (Effect of heat treatment on crystallization and mechanical properties of a hot-pressed lithium disilicate glass ceamic). T*ạp Chí Khoa Học Và Công Nghệ - Viện Hàn Lâm Khoa Học Công Nghệ Việt Nam, 53*(2A), 62-72.
19. Wen G., Zheng X., Song L. (2007): Effects of P_2O_5 and sintering temperature on microstructure and mechanical properties of lithium disilicate glass-ceramics. *Acta Materialia, 55*(10), 3583-3591. doi:10.1016/j.actamat.2007.02.009
20. Huang S., Li Y., Wei S., Huang Z., Gao W., Cao P. (2017). A novel high-strength lithium disilicate glass-ceramic featuring a highly intertwined microstructure. *Journal of the European Ceramic Society, 37*(3),1083-1094. doi:10.1016/j.jeurceramsoc.2016.10.020
21. Bai Y., Peng L., Zhu Q. (2017): The preparation of the lithium disilicate glass-ceramic with high translucency. *Journal of Non-Crystalline Solids, 457*, 129-134. doi:10.1016/j.jnoncrysol.2016.11.032
22. Mahmoud M. M., Folz D. C., Suchicital C. T. A., Clark D. E. (2015): Estimate of the crystallization volume fraction in lithium disilicate glass-ceramics using Fourier transform infrared reflectance spectroscopy. *Journal of the European Ceramic Society, 35*(2), 597-604. doi:10.1016/j.jeurceramsoc.2014.09.004
23. Fuss T., Moguš-Milanković A., Ray C. S., Lesher C. Youngman E., R., Day D. E. (2006): Ex situ XRD, TEM, IR, Raman and NMR spectroscopy of crystallization of lithium disilicate glass at high pressure. *Journal of Non-Crystalline solids, 352*(38-39), 4101-4111.doi:10.1016/j.jnoncrysol.2006.06.038
24. Nesbitt H. W., et al. (2011): Bridging, non-bridging and free (O^{2-}) oxygen in Na_2O-SiO_2 glasses: An X-ray Photoelectron Spectroscopic (XPS) and Nuclear Magnetic Resonance (NMR) study. *Journal of Non-Crystalline Solids, 357*(1), 170-180. doi:10.1016/j.jnoncrysol.2010.09.031
25. Sreenivasan H., et al. (2020): Field Strength of Network-Modifying Cation Dictates the Structure of (Na-Mg) Aluminosilicate Glasses. *Frontiers in Materials, 7*, 267. doi:10.3389/fmats.2020.00267
26. Zhu H., Wang F., Liao Q., Wang Y., Zhu Y. (2020): Effect of CeO_2 and Nd_2O_3 on phases, microstructure, and aqueous chemical durability of borosilicate glass-ceramics for nuclear waste immobilization. *Materials Chemistry and Physics, 249*, 122936. doi:10.1016/j.matchemphys.2020.122936
27. Buchner S., Radtke C., Balzaretti N. M. (2013): Densification of Lithium Disilicate under High Pressure Investigated by XPS. *Open Journal of Inorganic Non-metallic Materials, 3*(2), 15-21. doi:10.4236/ojinm.2013.32004
28. França R., Bebsh M., Haimeur A., Fernandes A. C., Sacher E. (2020): Physicochemical surface characterizations of four dental CAD/CAM lithium disilicate-based glass ceramics on HF etching: An XPS study. *Ceramics International, 46*(2), 1411-1418.doi:10.1016/j.ceramint.2019.09.105.